

# Analysis and Model of Cortical Slow Waves Acquired with Optical Techniques

Marco Celotto <sup>1</sup>, Chiara De Luca <sup>1</sup>, Paolo Muratore <sup>1</sup> Francesco Resta <sup>2</sup>, Anna Letizia Allegra Mascaro <sup>2,3</sup>, Francesco Saverio Pavone <sup>2,4</sup> Giulia De Bonis <sup>5,\*</sup> and Pier Stanislao Paolucci <sup>5</sup>

<sup>1</sup> Dept. of Physics, "Sapienza" University of Rome, Rome, Italy

<sup>2</sup> LENS, University of Florence, Florence, Italy

<sup>3</sup> Istituto di Neuroscienze, CNR, Pisa, Italy

<sup>4</sup> Dept. of Physics, University of Florence, Florence, Italy

<sup>5</sup> INFN, Rome, Italy

\* Correspondence: giulia.debonis@roma1.infn.it

Received: date; Accepted: date; Published: date

**Abstract:** Slow waves (SWs) occur both during natural sleep and anesthesia and are universal across species. Even though electrophysiological recordings have been largely used to characterize brain states, they are limited in the spatial resolution and cannot target specific neuronal population. Recently, large-scale optical imaging techniques coupled with functional indicators overcame these restrictions. Here we combined wide-field fluorescence microscopy and a transgenic mouse model expressing a calcium indicator (GCaMP6f) in excitatory neurons to study SW propagation over the meso-scale under ketamine anesthesia. We developed "de novo" a versatile analysis pipeline to quantify the spatio-temporal propagation of the SWs in the frequency band  $[0.5, 4]$  Hz. Moreover, we designed a computational simulator based on a simple theoretical model, which takes into account the statistics of neural activity, the response of fluorescence proteins and the slow waves dynamics. The simulator was capable of synthesizing artificial signals that could reliably reproduce several features of the SWs observed *in vivo*. Comparison of preliminary experimental and simulated data shows the robustness of the analysis tools and its potential to uncover mechanistic insights of the Slow Wave Activity (SWA).

**Keywords:** Slow Wave Activity; GCaMP6f; Wide-field Microscopy; *in vivo* Imaging; Data Analysis Methods; Toy-Model Simulation

## 1. Introduction

The phenomenon of slow cortical waves (*delta waves*) is a regime of brain activity that is observed in all mammals in a state of deep sleep or under anaesthesia. It is characterized by a large-scale collective activation of groups of neurons, with a characteristic undulatory space-time pattern. Slow waves appear to propagate on the cortex modulating the spiking frequency of the underlying neurons populations. More specifically, as a slow wave passes, the involved neurons transit from a state of low spiking activity (*down-state*) to a more intense one (*up-state*). This behaviour is so evident that it was among the first forms of neural activity to be recognized. The earliest descriptions of the event date back to the 1930s and were carried out by W. Gray Walter [1]. He observed delta waves through an electroencephalogram (EEG), an instrument invented by Hans Berger in 1924 [2]. Since then, many experimental studies have been conducted on the large-scale activity of neuronal populations. These studies have permitted to observe the brain moving between various states of activity, according to the cognitive state of the subject. The awake activity is distinguished from sleep, which is in turn subdivided into the REM stage (when the brain activity is more similar to the awake state than to the other stages of sleep) and in 3 non-REM stages [3]. The sleep stages transition is cyclical and it is repeated several times (normally 4 – 5) per night, starting from the REM and moving progressively from the first NREM stage (the lighter) to the third (the deepest). Each state of the brain activity

is characterized by the dominance of oscillations (alpha, beta, gamma, delta, theta) in the different regions of the frequency spectrum, in particular:

- **Wakefulness and REM phase:** *alpha waves*, in the frequency range [7.5, 12.5] Hz; *beta waves*, in the frequency range [12.5, 30] Hz; *gamma waves* in the > 30Hz band.
- **NREM, Stage 1:** *sleep spindles*, i.e. short volleys – the typical duration of the fusiform envelope of the oscillations is a few seconds – of high frequency (10 – 12 Hz) nervous activity.
- **NREM, Stage 2:** *K-complexes*, i.e. peaks of isolated and very large activity that occur for a short time duration, separated from each other by time intervals of a few minutes.
- **NREM, Stage 3:** *delta waves*, in the lowest part of the frequency spectrum ([0.5, 4] Hz).

In recent years, the comprehension of both the dynamics and the functional role of delta waves significantly improved. Current studies outline two complementary roles of slow waves, respectively implemented by the down-states and the up-states of neural populations [4] [5] [6]. According to these studies, the down-states would help neurons to rest, favoring their prophylactic maintenance; in other words, they would guarantee the restorative function of sleep [4]. On the other hand, studies on sleep deprivation show how it has negative consequences on many cognitive functions, such as memories consolidation and psychomotor vigilance [5]. The up-states would have a fundamental role in learning: the induction of spikes with appropriate temporal delays between pre- and post-synaptic neurons would trigger the mechanism of synaptic plasticity, enhancing and weakening the synaptic efficacies in order to encode the memories acquired during wakefulness [6] [7].

Up to the present, acquisition through electrodes – scalp electroencephalography (EEG) and intracranial electro-corticography (ECoG) – have been the standard methods for collecting slow waves data. Through them it is possible to record a signal related to the collective electric activity of populations of neurons. Via this kind of recordings, the presence of undulatory signals propagating regularly along the brain cortex is distinctly detectable. The dataset analyzed in this work consists of optical data instead. Raw data are images representing the optical signals generated by  $\text{Ca}^{2+}$  ultra-sensitive fluorescent proteins; proteins are present in the mouse neural system as a result of a genetic encoding; calcium concentration in the nervous system is correlated in many ways to the neurons populations activity [8]. The images have a higher spatial resolution than the data obtained from grids of electrodes, whereas the temporal resolution is much lower [9] [10].

In spite of the low sampling frequency and the convolution with the relatively slow fluorescence transfer function, pixels intensity modulation during time is eye-visible. The goal of this work is to quantify this effect and to observe, in it, the characteristic correlations of an undulatory collective behaviour in the frequency band of interest. We could then interpret the signals as a sign of slow waves, achieving our aim of observing delta waves propagation through optical techniques. The high spatial resolution results obtained from this approach could be employed as a key ingredient for data-driven simulations of the cortex dynamics.

The analysis pipeline has been developed in Python<sup>1</sup>. Firstly, images are masked, removing their non-informative part (black borders), and transformed into numerical data matrices. The signal corresponding to the light intensity of each pixel is analyzed; the passage of a wave on a pixel is identified with the signal minima. The information about the wavefront of down- to up-state transitions is isolated and the presence of the sought type of spatio-temporal correlations is confirmed. Successively, in order to compare the different data sets at our disposal, quantitative measures are taken (points of origin, histograms of speed and neural excitability). We point up that the analysis sequence discussed in this work can also be applied, automatically, to the study of new samples acquired with similar optical techniques.

---

<sup>1</sup> Python Software Foundation. Python Language Reference, version 2.7. Available at <http://www.python.org> (accessed on Dec. 2018)

In parallel with the data analysis, we have written a program (in Python) to mimic the nervous activity underlying the experimental images. The simulator is initialized getting in input the sequence of down- to up-state transition times for each pixel. The nervous activity is then reproduced on the basis of a simple theoretical model, according to which neurons are thought as Poissonian emitters with a spiking frequency modulated by the activation state (up or down) of the neural population they belong to. The activity of each pixel is given by the sum of the signals coming from all the neurons in that pixel. The pixel signal is then convoluted with a transfer function, chosen to imitate the experimental fluorescence response. The synthesized signals are then studied through the same analysis pipeline developed for the treatment of the experimental data. A general consistency between the results obtained from the experimental samples and from the simulated ones can be interpreted as a validation of both the analysis procedure and the theoretical assumptions underlying the computational model. To recap, the hypothesis that we want to validate here is that the combined and integrated activity of many Poissonian variables, convoluted with an appropriate transfer function and subjected to a modulation of the emission frequency (occurring at proper times, extracted from experimental data), can reproduce signals whose shape is similar to that observed in experimental recordings.

## 2. Materials and Methods

In this paper, we discuss two different lines of work. The former consists in the analysis of experimental images: we will introduce a complete sequence of analysis capable of identifying the slow waves signal on the cortex. The latter consists in justifying the shape of the experimental signals through a simple theoretical model which takes into account the statistics of the neurons activity and the fluorescence response of the proteins encoded in the mouse brain. A simulator (in the following denoted as *Toy Model*) has been implemented to synthesize artificial signals based on this model. Afterwards, the artificial signals have been analyzed with the same pipeline developed for the experimental data. Within this section we describe the characteristics of the experimental data, then we present both the analysis pipeline and the Toy Model.

### 2.1. Experimental Techniques of Data Acquisition and Raw Data

Experimental data, acquired from mice, have been provided by LENS (European Laboratory for Non-Linear Spectroscopy<sup>2</sup>). All procedures involving mice were performed in accordance with the rules of the Italian Minister of Health (Protocol Number 183/2016-PR).

The dataset consists in a series of  $100 \times 100$  pixels *.tif* images spaced out by a time step of 40 ms (sampling frequency of 25 Hz). Each image covers a  $25 \text{ mm}^2$  ( $5 \text{ mm} \times 5 \text{ mm}$ ) area and offers a perspective from above on the brain cortex of two transgenic Thy1-GCaMP6f mice<sup>3</sup>.

The total collection time for each mouse is about 5 minutes (8 dataset of 1000 frames, each corresponding to an observation period of  $40 \text{ ms} \times 1000 = 40 \text{ s}$ ). A modern electrode grid has a spacing of  $500 \mu\text{m}$  between electrodes [10] and can reach a sampling frequency of 25 kHz when the signal from each channel is digitized [9]. Compared to this, the resolution of the technique that we are studying is much worse from a temporal point of view (25 Hz for the optical technique, up to 25 kHz for the electrode grid) but spatially more refined ( $50 \times 50 \mu\text{m}$  pixels for the optical technique,  $500 \mu\text{m}$  interspaced electrodes for the grid).

In every analyzed image the left cerebral hemisphere of the anaesthetized mouse is clearly visible, while the incomplete parts of the right hemisphere have been cut, if present, at the beginning of the analysis pipeline. In Figure 1 a sample image is superimposed on the atlas of a mouse's brain cortex so that it is possible to recognize different cortical areas in the data. The hemisphere is surrounded by a black background, that has been masked during the analysis since not informative.

<sup>2</sup> LENS Home Page, <http://www.lens.unifi.it/index.php> (accessed on Dec. 2018).

<sup>3</sup> For more details, see The Jackson Laboratory, Thy1-GCaMP6f, <https://www.jax.org/strain/025393> (accessed on Dec. 2018).

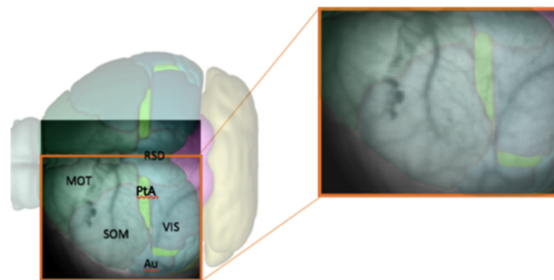


**Figure 1.** Representation of the mouse's cerebral cortex with overlapping names of the different areas: MOT = motor; SOM = somatosensory; Au = auditory; VIS = visual; PtA = associative parietal; RSD = retrosplenial dysgranular. The zoom shows which part of the cortex is visible in the raw data at our disposal.

Both mice are anaesthetized with a mix of Ketamine and Xylazine in doses of  $100\text{mg}/\text{kg}$  and  $10\text{mg}/\text{kg}$  respectively (milligrams of medicine per kilogram of the subject). Ketamine is an antagonist of the postsynaptic NMDA [11] receptors and the state induced by this anaesthetic is neurophysiologically different from natural sleep [12].

In Thy1-GCaMP6f transgenic mice, the CGaMP6f protein is genetically encoded. This protein is ultra-sensitive to calcium ions concentration [13] [14]; calcium concentration measurements are then correlated with the firing rate of neural populations underlying each pixel [8] [15].

The Thy1 gene is a promoter that allows the expression of the GCaMP6f indicator in the nervous system. The production of light signals from CGaMP6f is induced using the wide-field microscopy technique: when irradiated by a light source (in our case a LED light with a  $505\text{ nm}$  wavelength and  $4.94\text{ mW}$  power) the CGaMP6f protein emits a signal of fluorescence whose intensity is related to calcium ions concentration.  $\text{Ca}^{2+}$  ion flows in neural activity are some of the fastest in the organism [8][13]. Therefore it is necessary for  $\text{Ca}^{2+}$  indicators to have an adequately rapid response function. If compared to other genetically encoded proteins of the CGaMP family (obtained by assembling green fluorescent proteins, calmodulin and M13 [13]), CGaMP6f (f = fast) represents the best compromise between sensitivity and kinetic speed in the response to the presence of calcium (as shown by the light blue curve of Figure 1.(b) in [13]). Moreover, its sensitivity and speed of response are comparable to those of a synthetic calcium dye, such as OGB1-AM. However, the genetically encoded protein is much less invasive than synthetic dyes, which are injected directly into the brain tissue and are difficult to dispose of.

The passage of a slow wave over a neuronal population causes the spiking frequency of each involved neuron to move from  $\mu_{\text{down}}$  (in the down state) to  $\mu_{\text{up}}$  (in the up state). In this work it is assumed, as we will discuss in details in the following section, that the dynamics of the fluorescence response function is fast enough to identify, at least, the passage of down- to up-state wavefronts.

## 2.2. Data Analysis Pipeline

The data analysis pipeline has been coded in Python; in order to process the experimental data at our disposal, we have used the *scikit-image* package<sup>4</sup>.

The pipeline consists of three main sequences. The first concerns the image initialization and signal cleaning and is further subdivided into three parts:

- **Image initialization.** Each *.tif* image is imported and translated in a matrix of floats. Matrices are then assembled so that a collection of images belonging to the same recording set is stored in a 3D-array: 2 dimensions are spatial while the third is time (that is quantized in  $40\text{ ms}$  steps). Secondly, these data are manipulated in order to only keep informative content. Matrices are,

<sup>4</sup> Image Processing in Python, <https://scikit-image.org> (accessed on Dec. 2018).

therefore, manually cut in the spatial dimensions, isolating the portion of interest of the dataset (e.g. eliminating parts of the right hemisphere). According to the fact that the same image set shares the same perspective on the cortex, the cutting process is applied *en bloc* to each recording sample. Afterwards, in order to remove non-informative black edges from images, we make use of a masking process. The edges of the mask are obtained with the *find\_contours* function (*skimage.measure* Python package) which uses the *marching squares* algorithm. Finally, each pixel outside the mask is forced to take the *NaN* value (*Not A Number*).

- **Background subtraction and spatial smoothing.** Once the informative parts of the data are isolated, the pipeline proceeds with signal cleaning. The background is estimated as the mean of the signal for each pixel computed on the whole image set; it is then subtracted from images, pixel by pixel. Noise is further reduced with a spatial smoothing: pixels are assembled in  $2 \times 2$  blocks (*macro-pixels*); at each time, the value of a macro-pixel is the mean signal of the 4 pixels belonging to it<sup>5</sup>.
- **Spectrum analysis and time smoothing.** In order to identify the main frequency band in each dataset, a real Fourier transform (RFT) is computed for each pixel. A unique spectrum for the dataset is then obtained as the mean of single pixels' RFT. Given the mean dataset spectrum, the frequency band of maximum intensity is identified and the noise is further reduced by applying a 6° order band-pass Butterworth filter (provided by the *scipy* Python package<sup>6</sup>).

At the end of these preliminary steps, we obtain a 3D-array containing only the informative and cleaned signal. Subsequently, in order to normalize the information, the signal for each pixel is divided by its maximum value; the unit is therefore  $\frac{F-F_{back}}{F_{max}-F_{back}} \equiv \frac{\mathcal{F}}{\mathcal{F}_{max}}$ .

The second part of the analysis consists in finding the collection of up-state transition times for each pixel and in dividing the set of transition times into waves. We assume that it is possible to recognize the trigger of a transition to a collective up-state in the signal's minima of each pixel. This hypothesis is justified by the response function having a characteristic rise time  $\tau_{rise} \sim 150ms$  [13], comparable with the theoretical minimum time interval between the passage of two waves on a pixel<sup>7</sup>. Indeed, assuming to have two different waves emitted in antiphase with a temporal distance of  $250ms$  – slow waves maximum frequency is  $4Hz$  – the same neural population might be involved in the passage of two wavefronts in just  $125ms$ . Taking into account these borderline cases, the actual sub-band where the phenomenon is observable is  $[0.5, 3.3]Hz$ <sup>8</sup>. As long as the studied signal is part of this sub-band, the developed technique is able to detect the down- to up-state transition dynamics of a neuronal population throughout its whole duration. In this frequency range, indeed, as a wave is passing on a population, the corresponding signal is already decaying: the wave passage causes its ascent and, therefore, a local minimum of the signal. According to this hypothesis, it is possible to catch the quick transitions from down- to up-states with optical techniques characterized by fluorescence response times, thus much slower than the transition times themselves.

The analysis of minima has been developed by us from scratch; it can be divided into two steps:

- **Searching of minima.** The signal's temporal minima for each pixel are identified: this is done comparing the intensity value at each instant to its previous and next one.
- **Parabolic interpolation of minima.** A parabola is fitted around each minimum. All the 3 parabola's parameters are saved into a proper data structure. From the vertex of the parabola the interpolated time of the minimum (between original frames) is obtained. It is now possible to

<sup>5</sup> From now on, *macro-pixel* is meant each time *pixel* is mentioned.

<sup>6</sup> Scientific Python, <https://www.scipy.org> (accessed on Dec. 2018).

<sup>7</sup> This assumption, made for the wave rise time, is not valid for the decay time because the transfer function's decay time is  $\tau_{decay} \simeq 500ms$  [13]

<sup>8</sup> As better explained afterward, the profound anesthesia state causes the signal of interest to belong to this frequency sub-band.



reconstruct the activity of the minima at each time, following their movement both in time and space, as we will show in *Results* (Section 3).

Once the collection of minima of the whole dataset is obtained, it is partitioned into slow waves. The collection is given as an input to a MATLAB<sup>9</sup> pipeline developed by M. Mattia (Istituto Superiore di Sanità) and refined by G. De Bonis. This pipeline has already been used to analyze and elaborate data from electrodes [16] [17]. The first part of this pipeline – called *WaveHunt* – splits the set of transition times into separate waves. In order to do this, it is necessary to set an initial maximum time interval (*Time Lag*) between transitions, so that they can be labelled as part of the same wave. This value is iteratively reduced of the 25% until every identified wave respects the unicity principle: every pixel cannot be involved more than once from the passage of a single wave. We will only keep waves for which at least the 75% of the total pixels are involved (*global waves*). This selection is done in order to guarantee that what we call “wave” is actually a global collective phenomenon on the cortex. At the end of this step, we have all the down- to up- transition times (the minima) divided into waves.

Now, it is possible to get to the third part of the analysis pipeline, where quantitative information on the slow wave activity is obtained. In this phase, three different types of measures are taken:

- **Excitability of neuronal populations.** For each minimum the quadratic coefficient of the corresponding parabolic interpolation is taken. It is proportional to the concavity of the parabola, therefore it contains information on the excitability that the respective neural population exhibits as a response to the wave that is passing. The excitability unit is  $\left[ t^{-2} \cdot \frac{\mathcal{F}}{\mathcal{F}_{max}} \right]$ . In order to study the distribution of excitability, data are collected within a histogram. In addition to this, a graphical representation of pixel by pixel average excitability on the cortex is given (*excitability map*)<sup>10</sup>.
- **Wave Origin Points.** Once global waves are identified, the starting times of each wave are collected, identifying the first  $N$  pixels on which the wave has passed; in our case the choice is  $N = 30$ . These pixels select the region in which the wave has originated. The aim of this procedure is to make a statistics of the origin points.
- **Wave velocity.** In order to obtain the average speed of each wave, the wave velocity is calculated on different points. If the wave passage time function  $T(x, y)$  is known, the velocity of a wave on a point  $(x, y)$  can be defined as the inverse of the module of function’s gradient,

$$v(x, y) = \frac{1}{|\nabla T(x, y)|} \quad (1)$$

Computing the gradient and taking its module, we obtain:

$$v(x, y) = \frac{1}{\sqrt{\left(\frac{\partial T(x, y)}{\partial x}\right)^2 + \left(\frac{\partial T(x, y)}{\partial y}\right)^2}} \quad (2)$$

It should be noted that the function  $T(x, y)$  represents the wave passage time (in our case, the time of the minimum signal) in the spatial continuum. On the other hand, we only have this information for the discrete points corresponding to the pixels. For this reason, the partial derivatives that appear in (2) have been calculated as finite differences, with the distance between two pixels denoted as  $d$ :

<sup>9</sup> MATLAB®, The MathWorks, Inc., Natick, Massachusetts, United States, <https://www.mathworks.com/products/matlab.html> (accessed on Dec. 2018).

<sup>10</sup> It should be noted that the information on the excitability can also be obtained without subdividing the collection of minima into global waves. Indeed, the WaveHunt step is only necessary to obtain origin points and velocity. This is clearly shown in the flowchart at the end of this section (Figure 2), in which the logic of the whole pipeline is represented in a schematic form.

$$\left\{ \begin{array}{l} \frac{\partial T(x,y)}{\partial x} \approx \frac{T(x+d,y) - T(x-d,y)}{2d} \\ \frac{\partial T(x,y)}{\partial y} \approx \frac{T(x,y+d) - T(x,y-d)}{2d} \end{array} \right. \quad (3)$$

In performing these calculations, for each wave, only pixels having the adjacent 4 on which a transition occurs are taken into account; these are pixels for which it is possible to evaluate both the  $\frac{\partial T(x,y)}{\partial x}$  and the  $\frac{\partial T(x,y)}{\partial y}$ . By averaging the velocities over pixels that meet this condition, we obtain the average velocity of a wave; this procedure is repeated for each wave, in order to create a histogram of average wave speeds.

Through these measures we have been able to quantitatively compare the data coming from the two different mice, and from the simulation obtained with the Toy Model. A flowchart of the whole analysis pipeline is presented in Figure 2.

### 2.3. Toy Model

The theoretical model underlying the realization of the simulator is based on simple conceptual assumptions. Python objects that define the simulation will be indicated with the *italic*. The system is schematized as a two-dimensional grid of *Pixels*. Width and height of the grid can be easily set to reproduce the characteristics of the experimental images. Each *Pixel*, being ideally the image of a macroscopic portion of the cerebral cortex, contains a large number of *Neurons*. Each *Neuron* is located at a variable depth relative to the cortex surface. *Neurons* are the true sources of the signal. In the simplest theoretical modelling, *Neurons* are treated as independent units, each holding an internal binary state; this state identifies the *Neuron* as active or idle. Each *Neuron* generates a Poissonian signal during the simulation, whose mean value is modulated by the activation state. The state of each *Neuron* is controlled by the state of the *Pixel* to which the *Neuron* is assigned. When a *Wave* passes on a *Pixel*, it gets activated, and consequently are activated the *Neurons* in it. Vice versa, the absence of a wave for a certain period is codified by an idle state.

Experimental evidences<sup>11</sup> indicate that the ratio between the active state firing rate  $\mu_{\text{up}}$  and the idle state firing rate  $\mu_{\text{down}}$  can be estimated within the interval:  $\frac{\mu_{\text{up}}}{\mu_{\text{down}}} \in [4, 8]$ . Considering these results, it is therefore reasonable to set as parameters  $\mu_{\text{up}} = 10 \text{ Hz}$  and  $\mu_{\text{down}} = 2 \text{ Hz}$  for each *Neuron*.

Each *Neuron* has an intrinsic time of permanence in the active state  $\tau_{\text{up}}$ , after which it returns to the idle state. To fix this parameter – univocal, for simplicity, for the entire population of *Neurons* – we looked at experimental evidences that place this parameter in a range  $\tau_{\text{up}} \in [150, 200] \text{ ms}$  [13]. Therefore we set  $\tau_{\text{up}} = 200 \text{ ms}$ . A *Pixel* is declared inactive when each of its *Neurons* is in an idle state.

In order to model the presence of the fluorescent protein, from which the luminosity signal is obtained, the signal produced by each *Pixel* undergoes a convolution with a fixed response function. Since the analytical form of the response function is unknown, we made a modelling choice based on experimental results.

In order to reproduce the trend of the 6f variety of the response function as reported in [13], we decided to use a Log-normal function, defined as

$$\text{Lognormal}(x; \mu, \sigma) = \frac{1}{x} \frac{1}{\sqrt{2\pi}\sigma} \exp\left(-\frac{(\ln x - \mu)^2}{2\sigma^2}\right) \quad (4)$$

This function depends on the set of parameters  $\mathcal{P} = \{\mu, \sigma\}$  and its shape varies with them. A first and significant constraint that the response function must respect is the agreement between the

---

<sup>11</sup> Research currently underway by G. De Bonis *et al.* [10] on electrophysiological signals obtained from a sample of eleven mice in anaesthesia by Isoflurane.

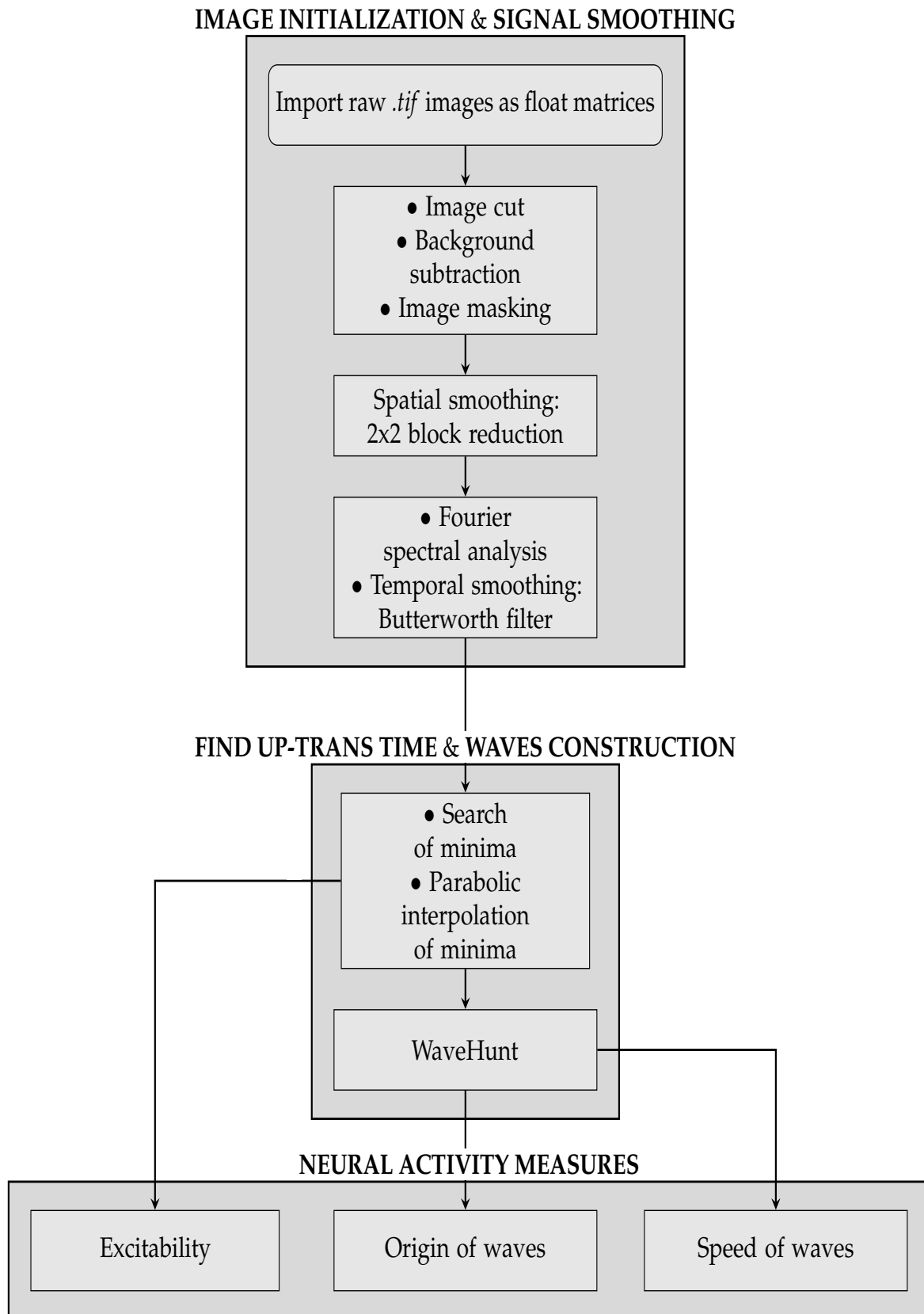


**Figure 2.** Flowchart of the analysis pipeline.



experimentally observed rise time  $\tau_{\text{rise}}$  and the modelled one. This value can be taken as the mode  $\mathcal{M}$  of (4); the following relation between parameters must therefore be respected:

$$\mathcal{M}[\text{Lognormal}] = \exp(\mu - \sigma^2) = \tau_{\text{rise}} \quad (5)$$

Looking at Figure in reference [13] it is possible to identify for  $\tau_{\text{rise}}$  a range of validity:  $\tau_{\text{rise}} \in [150, 200]$  ms. In order to be able to univocally identify the parameters  $\mu$  and  $\sigma$ , it would be necessary to impose a new constrain, for example a moment of the distribution. However, given the difficulty of extracting such an information visually, it was preferred to explore a set of reasonable values compatible with the constrain expressed in (5) and capable of reproducing as closely as possible the immediately visible characteristics of the function.

In Figure 3, a collection of Lognormal trends is plotted for different  $\{\mu, \sigma\}$  values that satisfy (5). Trends are normalized to  $\mathcal{F}_0$  – the median of the distribution – in order to facilitate the comparison between reports in [13] and Figure 3. This comparison shows important characteristics of the pair  $\mathcal{P}^* \equiv \{\mu = 2.2, \sigma = 0.91\}$ : the corresponding function, when decaying, halves its maximum value after a time interval of  $t_{\text{half}} = 0.5$  s, and reaches zero after about one second, mimicking the properties of the curve reported by [13] for the 6f variety. From these considerations it emerges that the pair of parameters  $\mathcal{P}^*$  is optimal for the description of the experimental response function, being able to reproduce the immediately observable characteristics of amplitude, asymmetry and tail weight. This set  $\mathcal{P}^*$  has then been used for the entire population of *Neurons*.

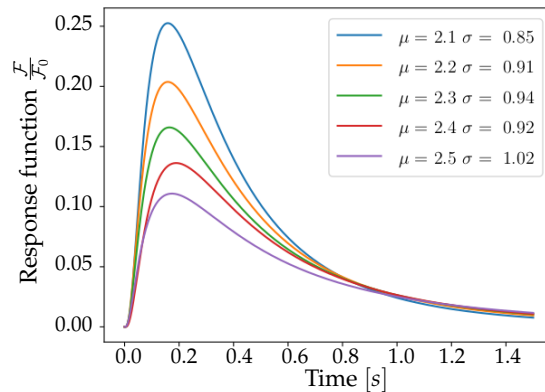


**Figure 3.** Lognormal functions for different set of parameters  $\mu$  and  $\sigma$ . The pair  $\{\mu = 2.2, \sigma = 0.91\}$  (in orange) is optimal for the emulation of curve 6f.

Once the simulation of Poissonian emitters is completed, each *Pixel* collects the sum of the signals produced by *Neurons* belonging to it. This population signal is then convolved with the just discussed Lognormal. The signal produced is the brightness signal of the whole *Pixel*. The sum of *Neuron* signals within the same *Pixel* is weighted by the depth parameter  $p$  of each *Neuron*, a value uniformly extracted in the interval  $I = [0, 1]$ : with the multiplication by  $p^2$ , a quadratic reduction of the *Neurons* contribution due to depth is achieved.

The number of *Neurons* in each *Pixel* has been extracted from a normal distribution  $\mathcal{N}(\mu = 10, \sigma = 2)$ , whose value is less than the real one due to the limited processing resources of the simulation.

Since the *Neurons* described in the Toy Model are intrinsically independent objects, no form of wave propagation or interaction would be possible. The dynamics is therefore implemented separately according to two different conceptual schemes. A first possibility consists in defining a certain number of waves during the simulation initialization. A wave is nothing more than an object defined on the two-dimensional grid with its own parameters of shape, position, velocity and acceleration. For each instant of time, the simulation evaluates the correct wave dynamics (processed according to the parameters previously specified) and checks the spatial overlap of waves and *Pixels*, assigning the activation status to each *Pixel*. Each wave is equipped with further parameters in order to make its

dynamics possibilities more flexible and broad; these parameters include an initial position of birth, a life time, a condition of reflection or absorption at the edges of the grid. A second possibility instead, developed for a more accurate comparison with the experimental data, consists in declaring a sequence of activation times for each *Pixel*. The simulation proceeds checking step by step which *Pixel* must be activated to respect the time sequences given in input.

On the next page, the logic implemented in the simulation – starting from the initialization phase up to the production of the final signal – is schematized in the form of a flowchart (Figure 4).

### 3. Results

This section shows the results of the analysis described in the previous section. Firstly, the results of the analysis carried out on the experimental data are presented, followed by the results obtained by applying the same pipeline on the numerical simulation data.

#### 3.1. Analysis of the Experimental Data

The first part of the previously described analysis is applied to raw images: these are imported as matrices of floating-point numbers, cut and masked, then the background is eliminated and the spatial smoothing is performed (macro-pixels). These steps can be seen in Figure 5. Moreover, in order to quantify the signal in units of  $\frac{F}{F_{max}}$ , for each macro-pixel, intensity values are divided by their own maximum.

Afterwards, each macro-pixel signal is analyzed in the frequency domain. The average spectrum of the dataset is computed as the mean of all macro-pixels spectra on time frames of 40 s; a sample is shown in Figure 6. The frequency range of interest is therefore selected and the signal is cleaned up via the 6<sup>th</sup> order band-pass Butterworth filter (time smoothing). According to a visual analysis of the spectra for both mice, a low-cut frequency  $\nu_{low} = 0.5$  Hz and a high-cut  $\nu_{high} = 3$  Hz have been chosen. This choice has been made because in the range  $\nu_{high} < \nu < \nu_{Nyq} = 12.5$  Hz<sup>12</sup> the spectral contributions appear small and equal on the whole band intensity, therefore they are identified as noise. The selected band falls in the *delta waves* reference band ([0.5, 4] Hz). It is assumed that the reason why  $\nu_{high} < 4$  Hz is because the doses of administered anaesthetic induce a deep state of anaesthesia in the mice. Anyhow,  $\nu_{high} = 3$  Hz implies that the activity of interest lies in the sub-band [0.5, 3.3] Hz, in which the assumptions made in Section 2.2 on the detectability of the down- to up-state wavefronts are valid. In Figure 7, a comparison between raw signal and clean signal is presented for a given pixel.

As discussed above, the minima of the signals are taken as reference of the passage of waves. By plotting signals in a certain time window for different channels (as in Figure 8), there is a visual confirmation that the nervous activity occurring in the frequency band selected by the filter has a non-trivial spatio-temporal correlation. By applying the minimum analysis pipeline presented in the previous section, we can study the slow waves dynamics. The collection of interpolated times of minima is obtained for each channel; the related parabolic fit parameters are saved. In this way it is possible to reconstruct, without the constraint of temporal discretization in steps of 40 ms, the activity of pixels that are transiting to the up-state or that have been recently activated (within a given time frame). From graphs of this type – such as those in Figure 9 – the wave propagation phenomenon appears evident.

A *raster plot* (Figure 10) is then produced: it offers a different perspective on the pixel activity: the transition times are plotted, as time passes, for each channel. Here, the presence of a collective and periodic, yet not stereotyped, activity stands out.

The WaveHunt algorithm, whose functioning is described in Section 2.2, splits the transition times collection up into global waves. Once this subdivision is completed and the triggering times

<sup>12</sup> For the Nyquist theorem, with a frequency of sampling  $\nu_{sampling} = 25$  Hz, we are able to reconstruct the frequency components of the signal up to  $\nu_{Nyq} = 12.5$  Hz.

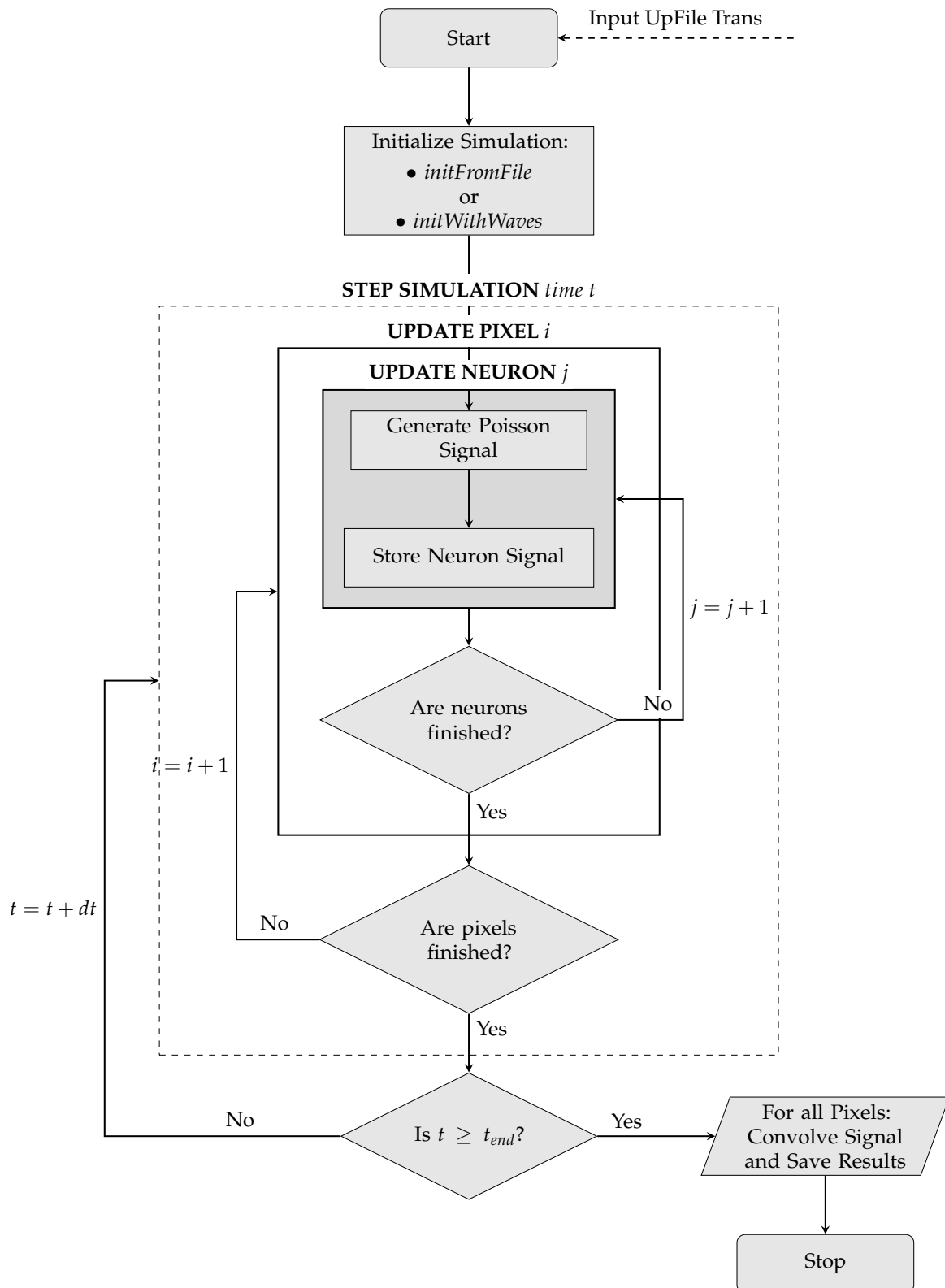
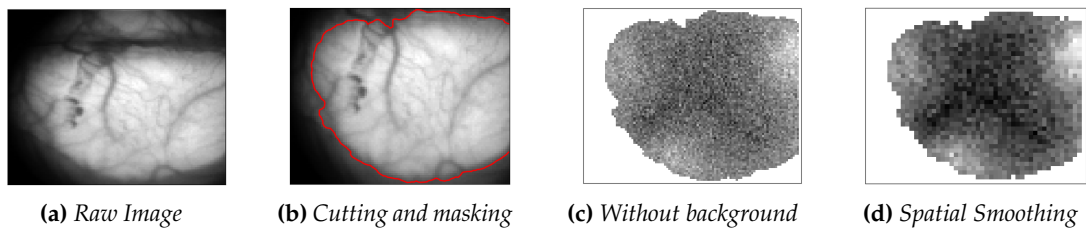
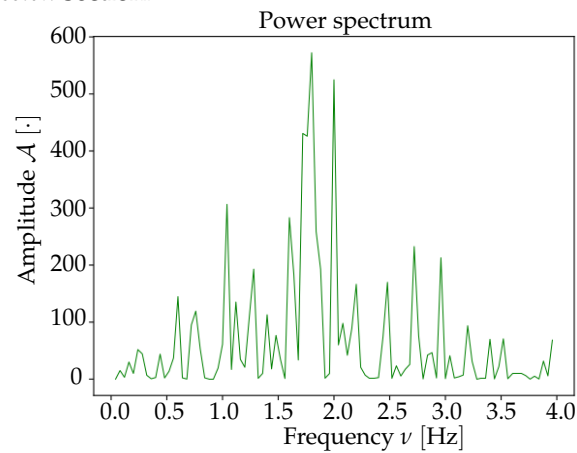


Figure 4. Flowchart of the simulation.



**Figure 5.** Image sequence showing the different steps of the signal cleaning process. (a) Example of a  $100 \times 100$  pixel raw image. (b) Image cut performed to exclude the non-informative area: only the left hemisphere has been selected (image size:  $100 \times 80$  pixels) and a mask has been created (specifically, 5564 out of 8000 original pixels are considered as signal sources). (c) Background is computed and subtracted from masked images. (d)  $2 \times 2$  macro-pixel spatial smoothing; the number of informative pixels is reduced to one quarter of the original ones (in this specific case, 1391 macro-pixels are obtained).

of each wave are known, all data necessary for moving to the last part of the analysis are obtained. The quantitative measurements described in *Materials and Methods* can now be taken. These will be examined in the *Discussion* section.



**Figure 6.** Average frequency spectrum calculated over a time frame of 40 s for a particular dataset (mouse referred to as *Keta1*).

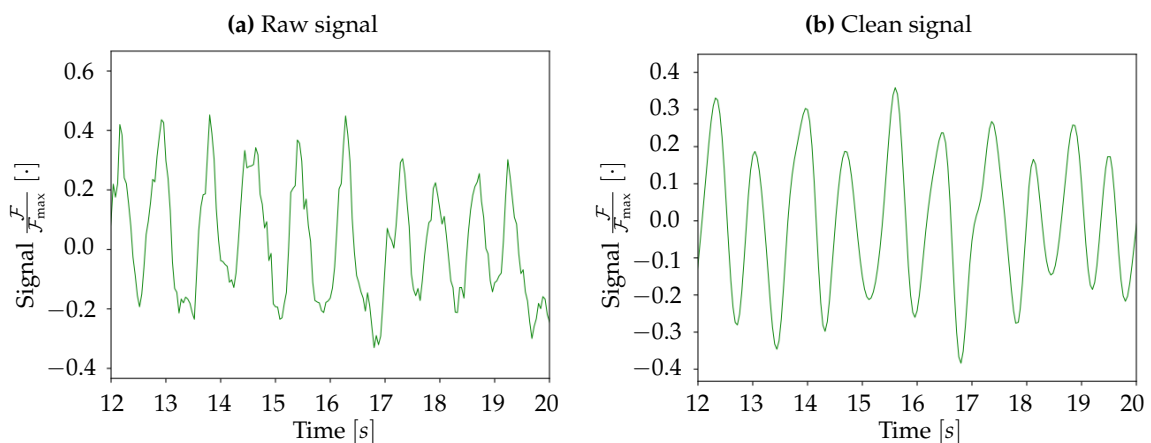


**Figure 7.** Comparison between 8 s of raw signal obtained from a given pixel (a) and the same signal cleaned through the application of the frequency filter (b).

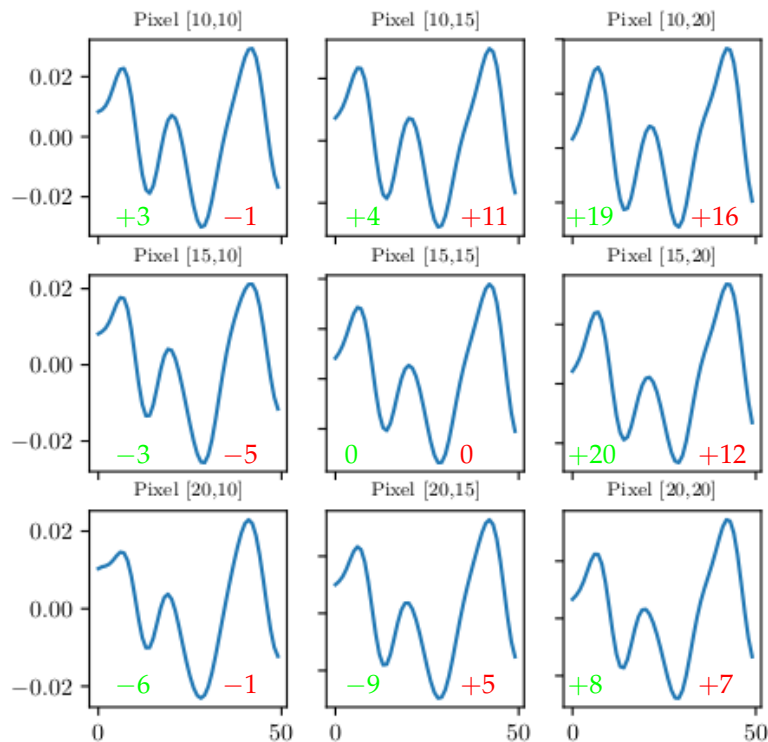


**Figure 8.** Neuron activity evaluated as  $\frac{F}{F_{max}}$  in the time frame  $[0, 50]$  frames (*i.e.*  $50 \times 40 \text{ ms} = 2 \text{ s}$ ) in different macro-pixels: the miniplot graphic layout reproduces the pixels spatial location on the hemisphere. On each miniplot, the time shift (in ms) from the first minimum of the central pixel is shown in green, whereas in red it is shown the time shift from the second minimum.

### 3.2. Analysis of the Simulation

The purpose of the simulation is to generate a synthetic signal comparable with experimental data through the application of the same analysis procedures. This comparison aims at validating both the discussed analysis pipeline and the theoretical assumptions underlying the Toy Model.

The signal is produced in successive steps. At the most basic level, every single neuron produces its own Poissonian signal with a firing rate that depends on the state of the neuron. This signal is then summed to the ones of the other neurons belonging to the same pixel, to form a pixel signal; the latter is then convolved with a kernel. An example of the Poissonian signal produced by a simulation neuron is shown in Figure 11; the single neuron signal is flanked by the one obtained convolving the pixel signal (to which the neuron belongs) with a LogNormal kernel<sup>13</sup>; the intensity value of the convolved signal is normalized to its maximum, in order to obtain an adimensional quantity. The response function control parameters  $\mu$  and  $\sigma$  have been chosen to obtain the highest agreement with

<sup>13</sup> To be precise, since the convolution operation is distributive, it does not matter whether it is made before or after summing the neuron signals. Therefore, although in Figure 11 a convolved pixel signal is shown, its shape will be very similar to the one of a convolved single neuron signal.

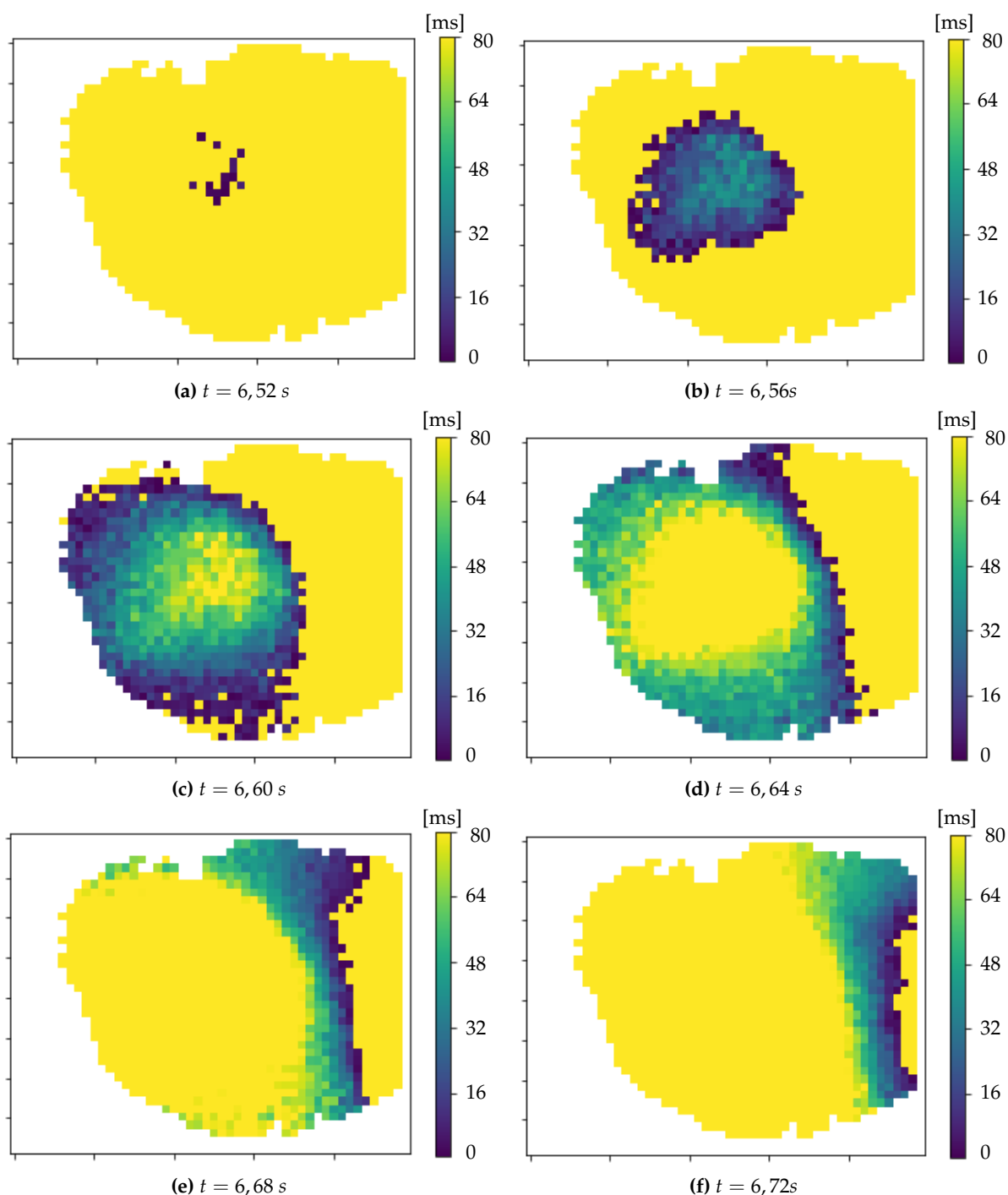


**Figure 9.** Series of images – interspersed with 40 *ms* time step – which shows the minima propagation front at different times. The global and correlated wave activity is evident. The pixels activated in the 80 *ms* preceding the time shown below each image are illuminated. The color represents the time elapsed from the up-ward transition: it goes from the dark blue for the pixels that have just turned on, to the green for those that have been activated almost 80 *ms* before the image capture time, up to the yellow for all the pixels whose neuronal population has not transitioned in the last 80 *ms*.



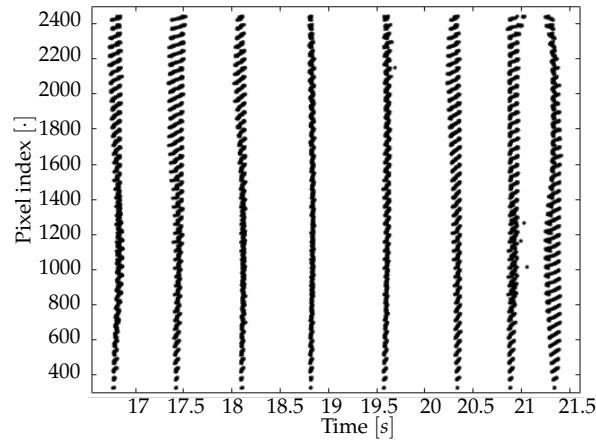


**Figure 10.** Raster plot of a time window for a particular data set. The presence of a global and regularly repeated activity of the system is clear, although each signal is characterized by different dynamics.

the experimental trend of the 6f protein. We recall the formula of the convolution kernel adopted in this work, specializing it with the parameters used for the simulation:

$$\text{Lognormal} \left( \frac{t}{t_{\text{step}}}; \mu, \sigma \right) = \frac{t_{\text{step}}}{t} \frac{1}{\sqrt{2\pi}\sigma} \exp \left( -\frac{\left( \ln \frac{t}{t_{\text{step}}} - \mu \right)^2}{2\sigma^2} \right) \quad (6)$$

where the time step of the simulation is indicated with  $t_{\text{step}}$ , its presence is necessary to make the time parameter adimensional (in our case  $t_{\text{step}} = 40 \text{ ms}$ ). The parameters chosen for the simulation are summarized in Table 1.

Parametro	Description	Value [unit of measurements]
$t_{\text{end}}$	Total time to simulate	Defined in input [s]
$t_{\text{step}}$	Simulation time step	40 [ms]
$\tau_{\text{up}}$	Neuron permanence time in active state	200 [ms]
$\mu_{\text{up}}$	Neuron Poissonian firing rate for the active state	10 Hz
$\mu_{\text{down}}$	Neuron Poissonian firing rate for the idle state	2 Hz
$N_{\text{pixel}}$	Neuron number for each Pixel	$N \simeq \mathcal{N}(\mu = 10, \sigma = 2)$ [.]
$\mu$	$\mu$ parameter of the LogNorm Kernel	2.2 [.]
$\sigma$	$\sigma$ parameter of the LogNorm Kernel	0.91 [.]

**Table 1.** Simulation parameters

In Figure 12 an extract of four simulation frames is shown. Each frame is separated from the previous one by a fixed time interval. The plot represents a two-dimensional  $50 \times 50$  pixels grid, ideally identifiable with an optical image of a cerebral cortex. The signal of each pixel is generated as previously described and the intensity is represented by a scale of normalized values.

As can be seen from Figure 11, the presence of a convolution with a response function having a non-zero rise time induces a measurable delay between the Poisson signal of the individual neurons and the brightness signal of the pixel. This effect would induce a low frequency anomalous component in the spectral decomposition of the simulated signal. This is the reason why the first ascent time

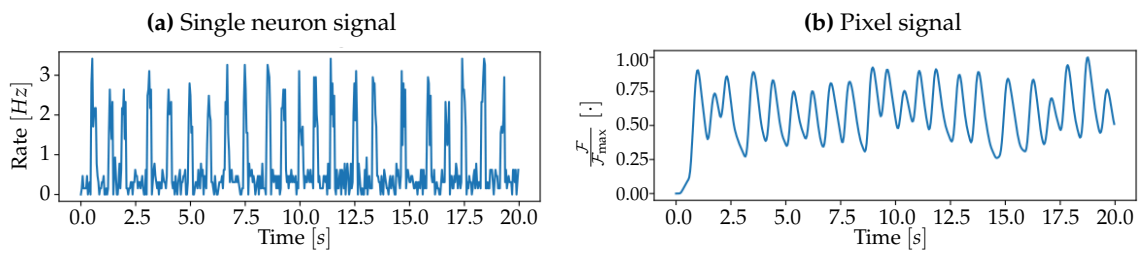


**Figure 11.** Signal generated by a single *Neuron* during a simulation (a), and the signal obtained from the corresponding pixel after the convolution with a LogNormal kernel of parameters  $\mu = 2.5$  and  $\sigma = 0.5$  normalized to the maximum value (b).

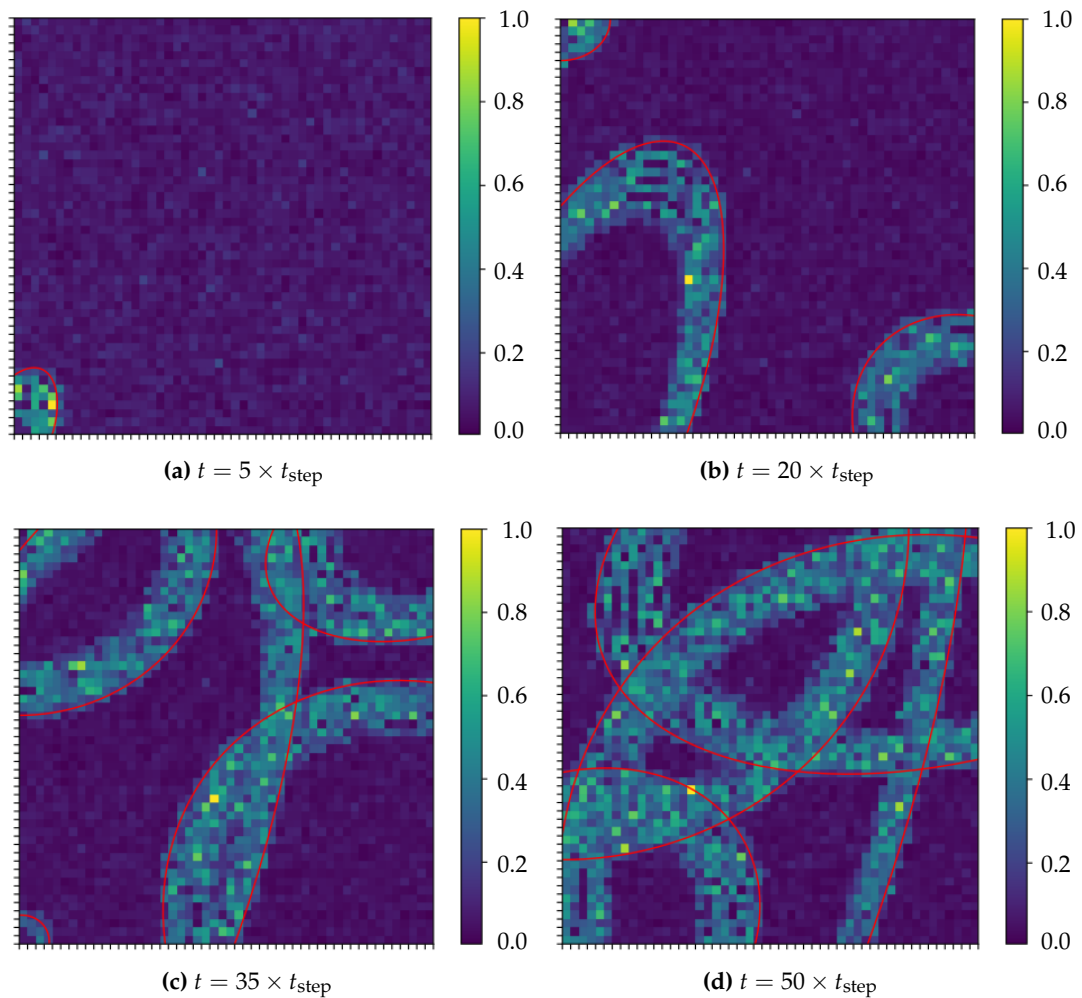


**Figure 12.** Sequence of four distinct frames of an elliptic waves simulation. In this embodiment, the wave propagation of five elliptic waves of different shapes and propagation velocities, generated at different times at the four edges of the domain, have been simulated. The red contours denote the wave front position in the time instant immortalized by the frame. The colour scale represents the strength of the signal, normalized to each time frame maximum value.

during the analysis in frequency has been discarded. After all, the experimental data are images of a neural cortex in activity, thus a possible period of initial rising of the light signal due to the initial activation of the network is absent, or in any case not measurable. By eliminating the first second of the simulation, a spectral trend in accordance with the experimental counterpart is recovered for the simulated signal.

## 4. Discussion

In this section, the comparison both between the analysis of different experimental realizations performed on the entire dataset, and between experimental samples and simulated data are presented and discussed.

### 4.1. Comparison between Experimental Samples

After its validation on a small portion of experimental data, the analysis pipeline described in the previous sections is applied to a larger sample: about 5 minutes of recordings for both mice at our disposal.

To proceed with the comparison of the data, we will refer to the two mice as *Keta1* and *Keta2*. In both mice, an oscillatory signal is observed in the delta waves reference frequency band. For the *Keta1* mouse, the main peak in the frequency spectrum is found at  $f_{\max} \simeq 1.7$  Hz (Figure 13a). Analogously, the Figure 13b illustrates the *Keta2* spectrum: the most intense frequency component is  $f_{\max} \simeq 1.9$  Hz. The spectral activity of the analyzed samples is, therefore, very similar. This similarity in the intensity of the frequency peak leads us to believe that other characteristics may be similar.

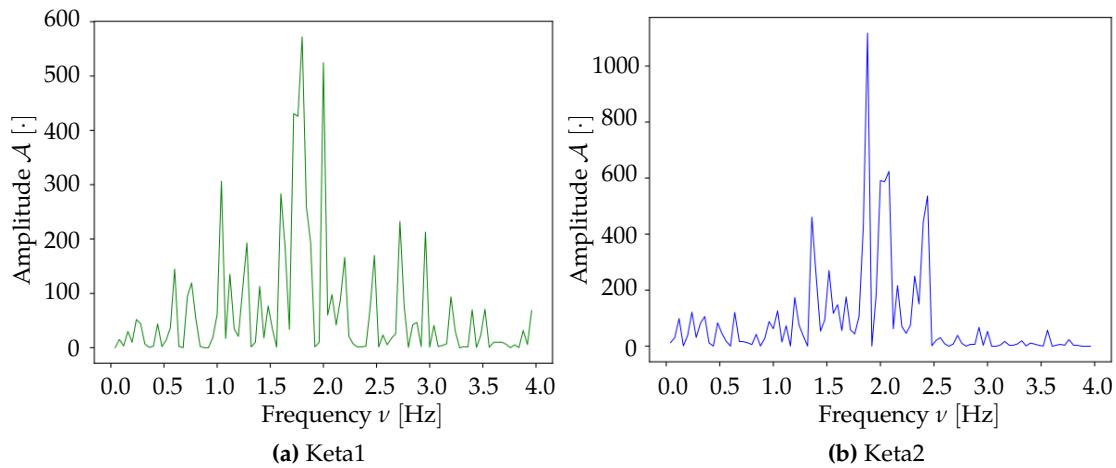


**Figure 13.** Comparison between the average frequency spectra of Keta1 (a) and Keta2 (b). Both samples present a peak at similar frequency values in the delta band.

The comparison between the graphs showing the points of origin of the waves (Figure 14a and 14b) shows a general analogy between the activity observed in Keta1 and in Keta2. In both samples, in fact, there is a prevalence of waves that are formed starting from the prefrontal cortex, although in Keta1 there is a spot of origin also in the posterior part of the cortex – indicatively in the retrosplenial area – and a wider distribution of points of origin in the frontal cortex.

Performing the study of the average wave propagation speed, we obtain the two histograms represented in Figure 15a and 15b. For Keta1, the waves average propagation speed is  $\langle v \rangle_{\text{Keta1}} = (26 \pm 8) \frac{\text{mm}}{\text{s}}$ ; for Keta2, the average speed is  $\langle v \rangle_{\text{Keta2}} = (30 \pm 8) \frac{\text{mm}}{\text{s}}$ . Not only these results are in agreement with each other, they are also consistent with other wavefront propagation measurements in the literature. For example, in [16], a study carried out using electrophysiological techniques, the average wave propagation speeds of  $\langle v \rangle = (30.0 \pm 3.9) \frac{\text{mm}}{\text{s}}$  and  $\langle v \rangle = (23.4 \pm 2.1) \frac{\text{mm}}{\text{s}}$  are reported for two mice anesthetized with a mix of ketamine (75 mg / kg) and medetomidine (1 mg / kg).

The coherence between the nervous activity of Keta1 and Keta2 is evident also looking at the comparison between the excitability histograms (Figure 16a and 16b). For Keta1, the average excitability is  $\varepsilon_{\text{Keta1}} = (1.0 \pm 0.6) \times 10^{-3} \text{ s}^{-2}$ , whereas for Keta2 the average excitability is  $\varepsilon_{\text{Keta2}} = (1.5 \pm 0.5) \times 10^2 \text{ s}^{-2}$ ; these two values are compatible with each other. The histograms also present a characteristic pattern with most of the neural population sharing excitability close to the unit, but with an evident asymmetry that denotes the presence of non-negligible high excitability tails.

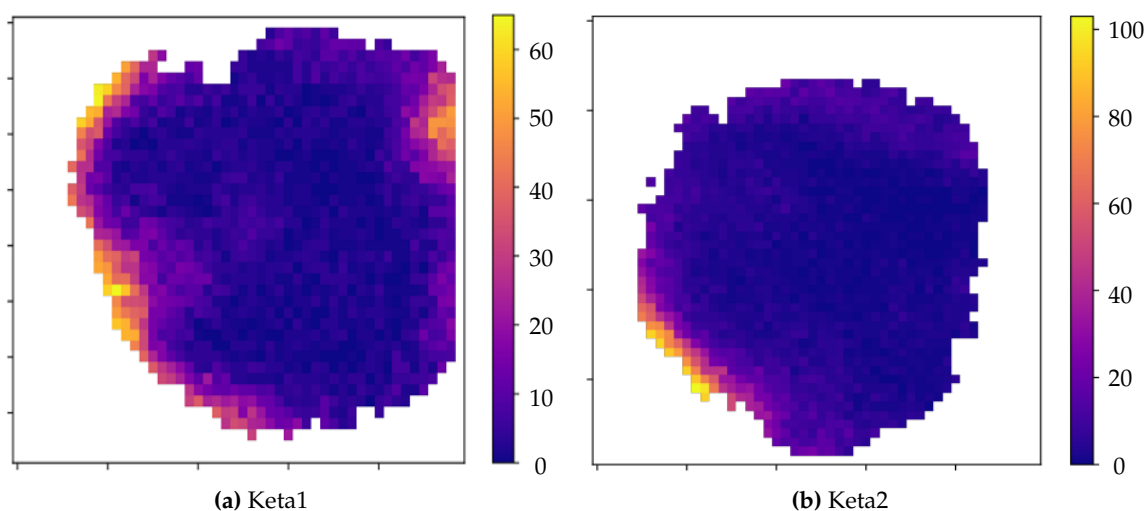


**Figure 14.** Maps of origin of the experimental waves for Keta1 (a) and Keta2 (b). The color code represents the number of times a single pixel has been involved in the birth of a global wave, defining the “birth set” as the first  $N = 30$  pixels on which each wave passes. Since in order to identify a wave as *global* we have decided that at least 1000 out of 1391 pixels should be involved, the “birth set” constitutes, at most, the 3% of the wave.

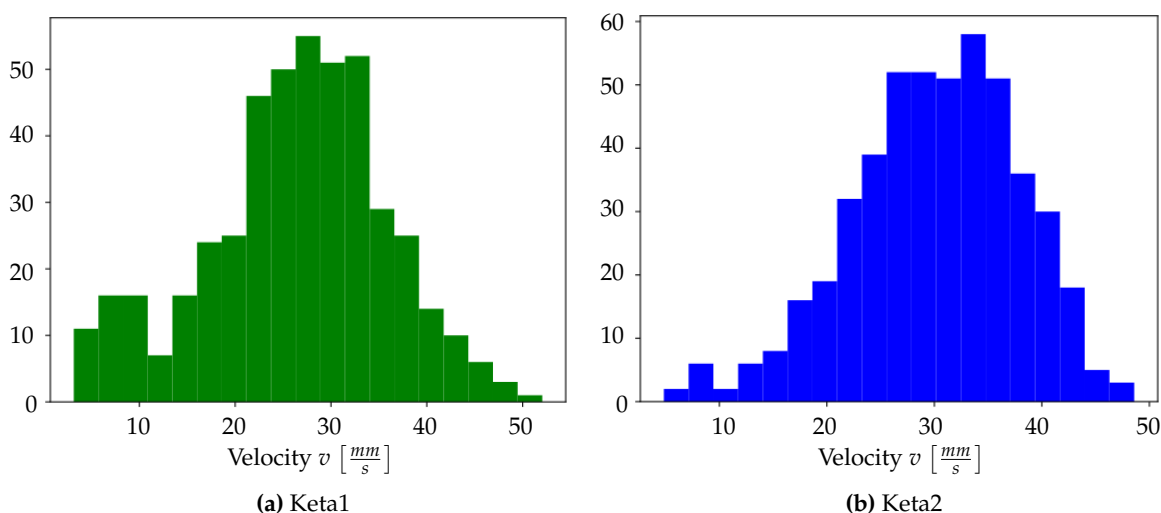


**Figure 15.** Histogram of the wavefront speed for Keta1 (a) and Keta2 (b).

Another type of graphical representation of the excitability data is shown in Figure 17a and 17b where the spatial dependence of this parameter is made explicit. In this case, the mean excitability on all the minima for each channel is performed, thus it can be observed how the mean excitability varies in the different areas of cortex. Both Keta1 and Keta2 show a peak of excitability in the central part of the cortex. In addition to this, the illustration allows to advance an hypothesis about the apparent excess of minima that have a minor excitability, as shown in the histogram of subject Keta1 of Figure 16a: this component could derive from the extended presence of superficial blood vessels (the dark spots in Figure 1) in areas where the cortex would show a higher excitability. The reduced number of observable neurons in these regions would explain a lower intensity rise due to the passage of waves; therefore, the signal would be wider and the second order parabolic coefficient would be smaller on these pixels; they would consequently be less excitable.

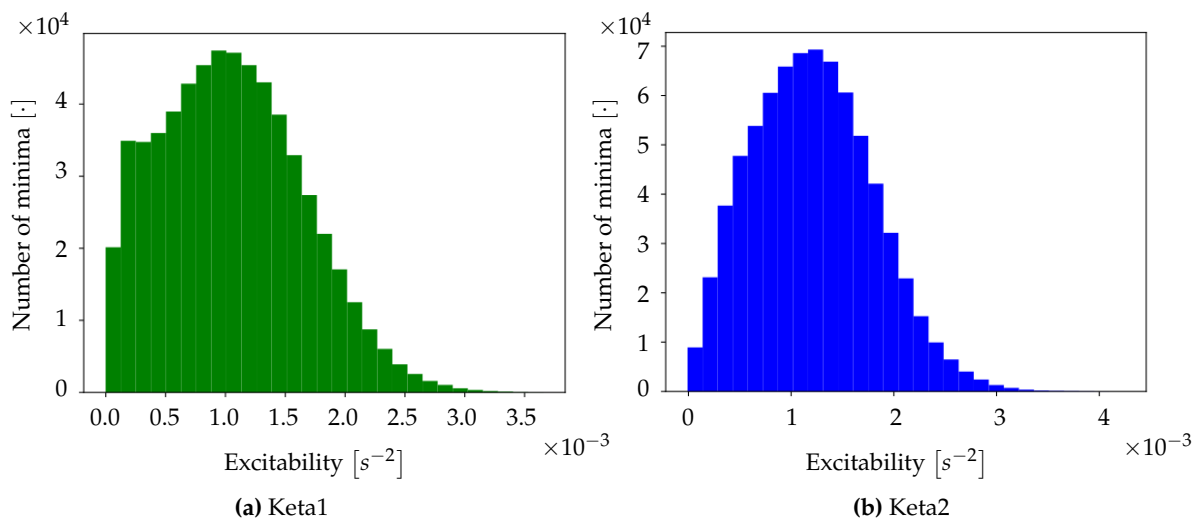


**Figure 16.** Histogram of normalized excitability for Keta1 (a) and Keta2 (b).

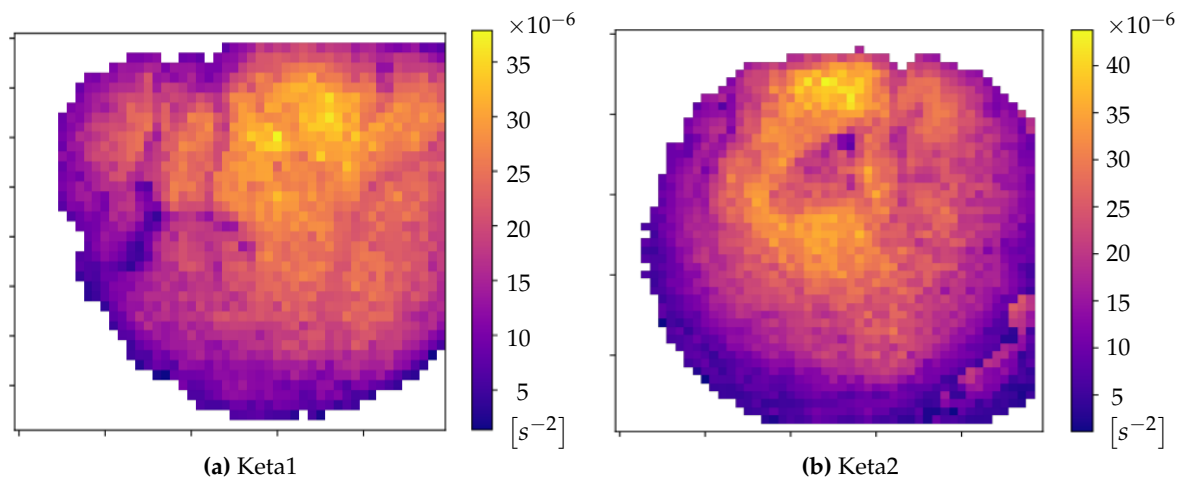


**Figure 17.** Maps of the cortex showing the average excitability per pixel for Keta1 (a) and Keta2 (b).

#### 4.2. Comparison between Experimental and Simulated Data

By using the experimental collection of transition times as a trigger for pixels of the Toy Model, it is possible to verify whether or not the simulation can reproduce experimental signals. This comparison has been made on a time frame of 40 s of experimental registrations (*i.e.* on a single dataset). As can be seen in Figure 18a and 18b, the agreement between the average frequency spectrum of the experimental signals and the one obtained from the Toy Model is very good. As already discussed in section 3.2, the simulated activity frequency spectrum has been obtained by eliminating the first second of simulation. This choice was made in order to avoid that the activation period of the Toy Model spoiled the spectrum, introducing a large component of low frequency that is not present once the simulation has reached its effective working regime. Moreover, as shown in Figure 19, the simulated signal shows a very convincing agreement with the one recorded *in vivo* from the mouse's cortex<sup>14</sup>. Results in Figures 18–19 validate the hypothesis that we made about the type of transfer function adopted to represent the fluorescence response of the CGaMP6f protein, which – we recall – is a Log-Normal. From the agreement between experimental and simulated signals there is, therefore,

<sup>14</sup> The signal produced by the simulation has been shifted by 2.93 ms to obtain Figure 19; this value follows by calculating the correlation function between the two signals.

a confirmation of how it is possible to detect the transitions from down to up neuronal states using optical techniques.

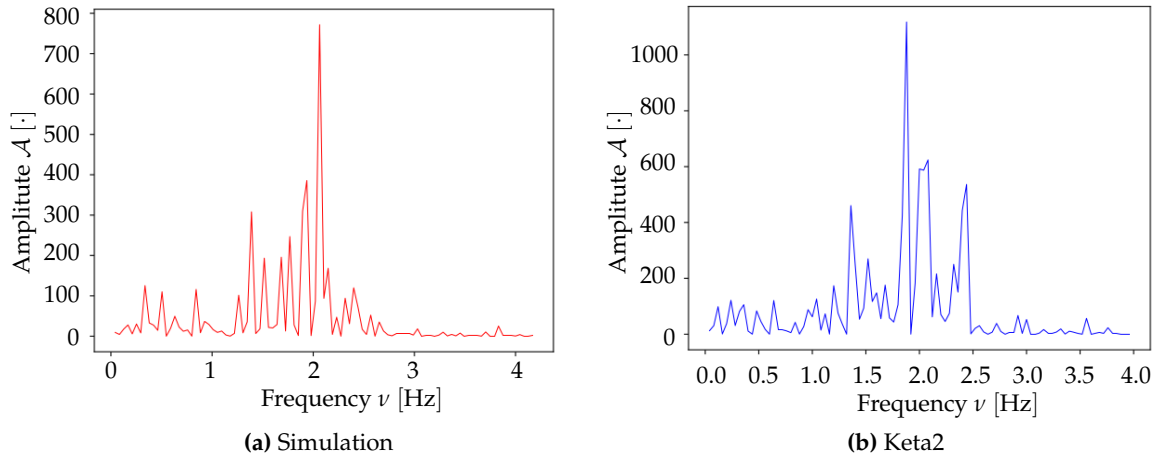


**Figure 18.** Comparison between the average frequency of the simulation (a) and the relative experimental spectrum on which the simulation has been based (b).

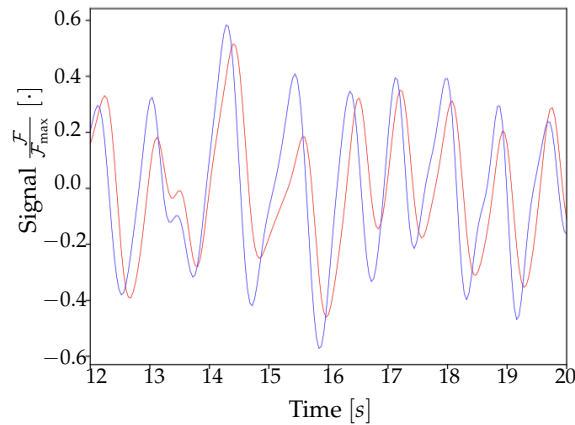


**Figure 19.** Comparison between the signal generated by the simulation, in red, and the related experimental signal, in blue, on a 8 s window for a single pixel.

The data produced by the Toy Model are subsequently submitted to the complete analysis pipeline: measurements of the mean velocity of wavefronts propagation and of neuronal excitability are obtained also for the simulation. In Figure 20a, 20b and 21 the results obtained by giving Keta2 transition times as input to the Toy Model are shown. Comparing the histogram of the Keta2 propagation speed (Figure 15b) with the simulated one (Figure 21), it is possible to observe how the one produced by the Toy Model is peaked around a different mean value – which is  $\langle v \rangle = (25 \pm 5) \frac{mm}{s}$  – resulting nonetheless compatible with the average speed of Keta2 within  $1\sigma$  error. This is indicative of the fact that the transitions timing sequence, associated with the Log-Normal transfer function, is sufficient to reproduce the experimental wavefront speed statistics.

As far as neuronal excitability is concerned, results appear to be substantially different from the original ones. The first evident discrepancy is illustrated by the spatial representation of the excitability, represented in Figure 20b, where there is no spatial dependence and a random pattern emerges. However, this behavior is understandable through the theoretical model underlying the simulation development. As described in the previous sections, modeled neurons are intrinsically non-interacting and highly stereotyped objects. Each neuron, in fact, shares parameters summarized in Table 1, and this implies that, as a wave arrives, all the neurons will respond with an equal change



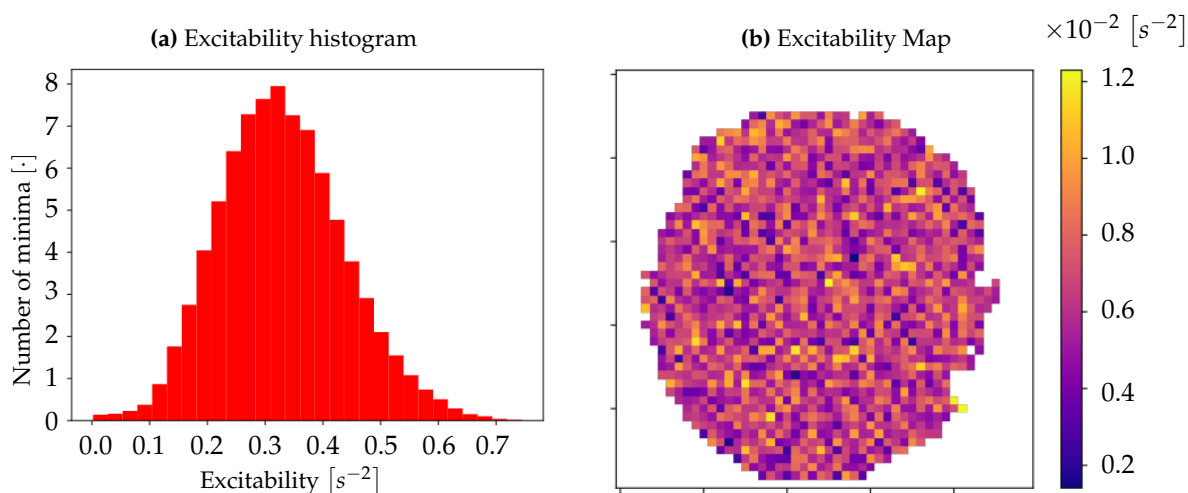


**Figure 20.** (a) Excitability histogram calculated on the artificial data; the corresponding spatial map is shown in (b).

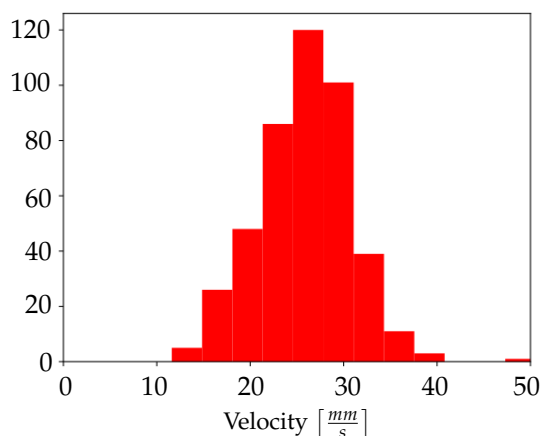


**Figure 21.** Histogram of the wave propagation speed for artificial data.

in the Poissonian rate, and then will produce a signal that will be convolved with the same transfer function. The only different feature is the randomness of the Poissonian process, which is not bound in any way to spatial reference. This is the characteristic that is reflected in the map of Figure 20b. The histogram of Figure 20a, whose trend appears to be Gaussian, supports this interpretation: this aspect is well explained by the Central Limit Theorem applied to the mean value of the excitability fluctuations (Poissonian), that are independent and summed up in the final average. Another important difference is in the absolute value of the measured excitability. Once again this aspect is a consequence of the modeling choices of the simulation: the speed of ascent is a parameter also influenced by the number of neurons present in a pixel, and this number is constrained by the computational resources and cannot compete with the high biological value. For this reason, the signals produced by the simulation have been compared with the respective biological signals after that both have been normalized. This operation removes the dissimilarities caused by the different number of neurons underlying the signals. However, normalization also affects the absolute values of excitability, stereotyping the depth of the minima and therefore the coefficients of the interpolating second order polynomial. The trend of the histogram should, in this sense, be interpreted as a validation of the intrinsic random character of the simulated model, rather than a reliable experimental measure of the values of excitability of the network.

Finally, the analysis of the waves origin points for the Toy Model have been omitted, as they are completely determined by the collection of transition times used as an input.

## 5. Conclusions

The work presented here is suitable for several possible future developments. A first step could be to compare the optical data with analogous measurements obtained through acquisitions from electrodes. In particular, we could run the complete analysis pipeline that was initially designed to study the cortical activity recorded through an electrode grid [16] [17]. The pipeline is easily adaptable, and the pieces of information needed are the number of channels under consideration, their mutual spatial location and the upward transition times for each channel. The first two depend on the nature of the analyzed data and are immediately accessible; the third one can be obtained as discussed in the previous sections. Once the collection of transition times is received in input, the program deals with splitting it up into waves, through the WaveHunt algorithm discussed in Section 2.2. Then, a *time lag matrix* is built: it contains the transition times of each channel (columns) for each wave (rows). A dimensional reduction of the parameter space is performed via PCA (Principal Component Analysis). In the small-sized space, a k-mean clustering is performed iteratively, varying the number of clusters to be identified. What obtained is that waves are collected in different categories based on similarity criteria. For each wave group, a mean wave is calculated and the corresponding wavefront is reconstructed at different time steps. In addition to offering a clear perspective on the different types of delta waves present (grouped in the same cluster), this procedure calculates the average speed of each wave cluster. The program can be executed starting from the collection of transition times that we obtain from the analysis of minima. In this way, a direct and quantitative comparison could be made between the types of waves detected from optical data and those observed through electrodes.

A further direction could be to apply the analysis pipeline discussed in this work to other data samples, in different neurophysiological states, in which slow waves are observed. With this approach, a quantitative comparison could be made on the type of delta waves that occur under different anesthetics (for example GABAergics such as propofol, isoflurane and sevoflurane).

Concerning the Toy Model developed for this study, it could be used to infer the fluorescence transfer function between the  $\text{Ca}^{2+}$  ion concentration and the measured optical signal. Assuming an analytical representation for the transfer function dependent on a set of parameters, it could be possible to train a decision algorithm, such as a neural network, to infer the parameters of the transfer function (rather than performing a standard deconvolution, that is often a complex operation). For this purpose, the training set could be obtained through the Toy Model, simulating signals for different set of parameters varying in certain reference ranges. Then, giving in input to the network the acquired experimental signals, this, if properly trained, would output the optimal parameters for the real transfer function.

The reconstruction of the wavefronts obtained from this type of analysis can also be useful for the estimation, with a high spatial resolution, of effective connectivity matrices – during the state of deep sleep – between the neural populations underlying the individual pixels.

Eventually, the spatio-temporal high-resolution characterization of SWA, enabled by the methods here described, will be essential to tune the parameters and the interconnect of spiking neural network simulations, like those empowered at similar spatio-temporal resolution by distributed engines [18]. This will overcome the limits of current simulations that use simplified and stereotyped assumptions, and it will make possible the validation of competing theoretical models, by matching simulations with experimental data.

**Author Contributions:** Conceptualization, F.R., A.L.A.M., F.S.P., G.D.B. and P.S.P.; methodology, all; software, M.C., C.D.L. and P.M.; investigation, F.R., A.L.A.M.; writing – original draft preparation, M.C., C.D.L. and P.M.; writing – review and editing, F.R., A.L.A.M., G.D.B. and P.S.P.; visualization, M.C., C.D.L. and P.M.; supervision, P.S.P. and F.S.P.; project administration, P.S.P. and F.S.P.; funding acquisition, P.S.P. and F.S.P.

**Funding:** This research was funded by the European Union’s Horizon 2020 Framework Programme for Research and Innovation under Specific Grant Agreements No. 785907 (HBP SGA2) and No. 720270 (HBP SGA1).

**Acknowledgments:** This study was carried out in the framework of the Human Brain Project (HBP<sup>15</sup>), funded under Specific Grant Agreements No. 785907 (HBP SGA2) and No. 720270 (HBP SGA1), in particular within activities of sub-project SP3 (“Systems and Cognitive Neuroscience”) and sub-project SP1 (“Mouse Brain Organization”). Part of this work has been submitted in fulfillment of the requirements for the final exam of the course of Physics Laboratory II (Biosystems) 2017–2018, held by Prof. Federico Bordi for the Master’s Degree in Physics, “Sapienza” University of Rome.

**Conflicts of Interest:** The authors declare no conflict of interest.

## References

1. W.G. Walter, *The electroencephalogram in cases of cerebral tumor* Proc R Soc Med 30 (1937) 579–598.
2. H. Berger, *Über das Elektrenkephalogramm des Menschen* Arch Psychiat Nervenkr 87 (1929) 527–570.
3. R.K. Malhotra and A.Y. Avidan, *Sleep Stages and Scoring Technique*. In S. Chokroverty, R. Thomas *Atlas of Sleep Medicine, 2<sup>nd</sup> Edition*, Saunders, an imprint of Elsevier Inc. (2013) 77.
4. V.V. Vyazovskiy and K.D. Harris, *Sleep and the single neuron: the role of global slow oscillations in individual cell rest*, Nat Rev Neurosci. 14 (2013) 443.
5. W.D. Killgore, *Effects of sleep deprivation on cognition*, Prog Brain Res. 185 (2010) 105.
6. B.O. Watson, D. Levenstein, J.P. Greene, J.N. Gelinas and G. Buszáki, *Network Homeostasis and State Dynamics of Neocortical Sleep*, Neuron 90 (2016) 839.
7. C. Capone, E. Pastorelli, B. Golosio and P.S. Paolucci, *Sleep-like slow oscillations induce hierarchical memory association and synaptic homeostasis in thalamo-cortical simulations*, arXiv:1810.10498.
8. C. Grienberger and A. Konnerth, *Imaging Calcium in Neurons*, Neuron. 73 (2012) 862.
9. W.S. Konerding, U.P. Froriep, A. Kral and P. Baumhoff, *New thin-film surface electrode array enables brain mapping with high spatial acuity in rodents*, Sci Rep. 8 (2018) 3825.
10. G. De Bonis *et al.*, *Slow Waves Analysis Pipeline for extracting the Features of the Bi-Modality from the Cerebral Cortex of Anesthetized Mice*, in preparation.
11. M. Irifune, T. Shimizu, M. Nomoto and T. Fukuda, *Ketamine-induced anesthesia involves the N-methyl-D-aspartate receptor-channel complex in mice*, Brain Res. 596 (1992) 1.
12. O. Akeju and E.N. Brown, *Neural oscillations demonstrate that general anesthesia and sedative states are neurophysiologically distinct from sleep*, Curr Opin Neurobiol. 44 (2017) 178.
13. T.W. Chen, T.J. Wardill, Y. Sun, S.R. Pulver, S.L. Renninger, A. Baohan, E.R. Schreiter, R.A. Kerr, M.B. Orger, V. Jayaraman, L.L. Looger, K. Svoboda and D.S. Kim, *Ultrasensitive fluorescent proteins for imaging neuronal activity*, Nature 499 (2013) 295.
14. H. Dana, T.W. Chen, A. Hu, B.C. Shields, C. Guo, L.L. Looger, D. S. Kim e K. Svoboda, *Thy1-GCaMP6 Transgenic Mice for Neuronal Population Imaging In Vivo*, Plos One 9 (2014) 9.
15. R. Yasuda, E.A. Nimchinski, V. Scheuss, T.A. Pologruto, B.L. Sabatini and K. Svoboda, *Imaging calcium concentration dynamics in small neuronal compartments*, Sci STKE. 2004 (2004) pl5.
16. M. Ruiz-Mejiasa, L. Ciria-Suarez, M. Mattia and M.V. Sanchez-Vives, *Slow and fast rhythms generated in the cerebral cortex of the anesthetized mouse*, Press. J Neurophysiol. 106 (2011) 2910.
17. C. Capone, B. Rebollo, A. Muñoz, X. Illa, P. Del Giudice, M.V. Sanchez-Vives and M. Mattia, *Slow Waves in Cortical Slices: How Spontaneous Activity is Shaped by Laminar Structure*, Cereb. Cortex (2017) 1.
18. E. Pastorelli, P. S. Paolucci, F. Simula, A. Biagioni, F. Capuani, P. Cretaro, G. De Bonis, F. Lo Cicero, A. Lonardo, M. Martinelli, L. Pontisso, P. Vicini and R. Ammendola, *Gaussian and Exponential Lateral Connectivity on Distributed Spiking Neural Network Simulation*, Proc. of 26th Euromicro International Conference on Parallel, Distributed and Network-based Processing (PDP), 2018, pp. 658-665; DOI:10.1109/PDP2018.2018.00110.

---

<sup>15</sup> <https://www.humanbrainproject.eu/en/>